Chaos, Solitons and Fractals 179 (2024) 114413

Contents lists available at ScienceDirect

Chaos, Solitons and Fractals

journal homepage: www.elsevier.com/locate/chaos

# Medium inhomogeneities modulate emerging spiral waves

Dorsa Nezhad Hajian [a], Fatemeh Parastesh [b], Sajad Jafari [a,c], Matjaž Perc [d,e,f,g,*], Eva Klemenčič [d,h]

[a] Department of Biomedical Engineering, Amirkabir University of Technology (Tehran Polytechnic), Tehran, Iran
[b] Centre for Nonlinear Systems, Chennai Institute of Technology, Chennai 600069, Tamil Nadu, India
[c] Health Technology Research Institute, Amirkabir University of Technology (Tehran Polytechnic), Tehran, Iran
[d] Faculty of Natural Sciences and Mathematics, University of Maribor, Koroška cesta 160, 2000 Maribor, Slovenia
[e] Department of Medical Research, China Medical University Hospital, China Medical University, Taichung 404332, Taiwan
[f] Complexity Science Hub Vienna, Josefstädterstraße 39, 1080 Vienna, Austria
[g] Department of Physics, Kyung Hee University, 26 Kyungheedae-ro, Dongdaemun-gu, Seoul, Republic of Korea
[h] Faculty of Energy Technology, University of Maribor, Hočevarjev trg 1, 8270 Krško, Slovenia

ARTICLE INFO

*Keywords:*
Spiral waves
FitzHugh–Nagumo
Inhomogeneity

ABSTRACT

We study the spatiotemporal dynamics of spiral waves in a lattice of chemically coupled memristive FitzHugh–Nagumo neurons. We also introduce local and global functional inhomogeneities by means of variations in nodal action potentials that are distributed in different ways. We find that, in the presence of globally distributed random inhomogeneity, increasing the maximum threshold for excitability generates neurons with reduced depolarization capacity. Although such a setup makes the entire medium less excitable and thus challenges the robustness of emerging spiral waves, highly excitable neurons can compensate for the less excitable ones, thereby nonetheless preserving the spiral wave pattern. However, this compensatory mechanism has limitations, which can ultimately lead to the elimination of spiral waves under specific conditions. When inhomogeneities are local, two different scenarios are possible. If the distribution is random, the spiral tip cannot penetrate the inhomogeneous region but remains resilient against it. The tip is consistently anchored to the inhomogeneity, meandering around its boundary. As the inhomogeneity size increases, the curvature of the spiral tip and the propagation speed of the circular wavefronts decrease. If the distribution is uniform, inhomogeneities are analogous to semi-conducting barriers, thus permitting the spiral rotor to penetrate while sacrificing the strength of its wavefronts.

## 1. Introduction

Excitable media serve as frameworks where complex spatiotemporal patterns can arise [1,2]. Many of these patterns display chiral structures [3], commonly recognized as spiral waves [4], and are manifested in two-dimensional settings [5]. These waves represent regimes of self-organization [6] and self-sustainability [7,8], frequently addressed in the kinetics of chemical reaction–diffusion [9] and the heart muscle [10]. A growing body of evidence indicates that the uninterrupted periodic activity of reentrant sites [11], namely spiral rotors, could be precursors to several severe cardiac arrhythmias [12].

In an ideally homogeneous medium, the spiral wave may rotate uniformly around a center, possibly defined by initial conditions. Yet, realistic biological tissues are more described as inhomogeneous media [13,14]. A stationary spiral wave anchored to a local inhomogeneity is assumed to drive cardiac fibrillation [11]. In such an inhomogeneous environment, kinematic parameters tend to be spatially dependent. Within the myocardium, inhomogeneity can be divided into structural and functional types. Structural inhomogeneity is exemplified by inhomogeneous fibrosis of the muscle [15], while variations in the duration of action potentials illustrate functional inhomogeneity [16]. The presence of neurons with varying levels of excitability within a network adds another layer of complexity to the analysis [17,18]. From the computational point of view, inhomogeneities can arise through various mechanisms [19,20]. Structural inhomogeneity can be realized by spatial variations in the diffusion coefficient of coupling [21], the number of nodal connections within a lattice [22,23], and the placement of defect blocks [24]. When inhomogeneity is applied to the nodal kinetics parameters, it is categorized as functional. An instance of functional inhomogeneity is discussed in Ref. [25], where the effects of a vortex electric current introduced by a spatially polarized field is assessed.

The parametric setting of the FitzHugh–Nagumo (FHN) model not only simulates a time-dependent firing mechanism in excitable nerve

* Corresponding author at: Faculty of Natural Sciences and Mathematics, University of Maribor, Koroška cesta 160, 2000 Maribor, Slovenia.
*E-mail address:* matjaz.perc@gmail.com (M. Perc).

https://doi.org/10.1016/j.chaos.2023.114413
Received 18 November 2023; Accepted 20 December 2023

cells [26,27] but also offers considerable computational flexibility [28]. Thus, many of its parameters can introduce inhomogeneity [29]. For example, reducing the parameter responsible for the current inhibition resulted in immediate depolarization [15,30]. Similar effects can be achieved by modifying the model's relaxation parameter [23]. In other neuronal models, inhomogeneities in the conduction properties of models with explicitly defined channels have also been studied [31].

Distinct scenarios were observed when inhomogeneities were introduced to the medium. Localized inhomogeneity can induce and sustain coherent spiral waves [29]. This effect is frequently linked to the attachment of the spiral rotor to the inhomogeneity site, known as pinning or anchoring [32–36]. Another potential scenario involves the drift of spirals [37,38], especially when considering a gradient within the spatial arrangement of inhomogeneity [39,40]. Moreover, inhomogeneity can also cause spiral waves to break into multiple spirals with varying rotation speeds [13,41], analyzed from a wavelet perspective [15].

In the present work, a lattice of chemically coupled memristive FitzHugh–Nagumo neurons is realized. The model's relaxation parameter is chosen as the inhomogeneity parameter. As this parameter differs, the dynamic responses of neurons to stimuli manifest either as sustained depolarization in a plateau-like manner or a rapid damping response. Global and local cases are assessed for the spatial setting of inhomogeneity. To our knowledge, minor perturbations in the excitability of neurons across the entire lattice have seldom been addressed. Therefore, the initial section of our results concentrates on evaluating global functional inhomogeneities that are stochastically distributed, which is in line with existing literature [42]. We then evaluate the resilience of emerging spirals to increased variations in this stochastic distribution. Although the literature on the effect of local inhomogeneity is rich, we have focused on a distinct perspective in this work. Our primary objective is to identify which inhomogeneous regions can be penetrated by the spiral tip. We then investigate types of local inhomogeneities: one with a random distribution of excitability-tuning parameters and another with a uniform distribution. If pinning occurs, a phenomenon anticipated based on existing literature, we further examine the secondary effects of pinning in terms of the propagation speed of wavefronts.

The novelty of our research primarily resides in evaluating spirals with varying characteristics, including spirals with denser propagating waves resulting from a more curved reentrant tip and those with less frequent wavefronts. Additionally, these propagating wavefronts can differ in strength, evident in the thickness of the circular traveling wavefronts.

The remainder of this paper is structured as follows: Section 2 explores the nodal dynamics and parameter implementation. It also presents the synaptic connections and initial conditions required to generate single-core and centered spiral waves with varying characteristics. Additionally, this section illustrates the nodal responses concerning changes in relaxation parameters to elucidate the effects of inhomogeneity on the collective behaviors observed in subsequent sections. Section 3 presents the results of spiral waves when the medium exhibits three distinct scenarios of inhomogeneity. Section 4 briefly discusses the underlying mechanism of pinning in the case of local inhomogeneity. Lastly, the final section provides the paper's conclusion.

## 2. Methods and models

This section is organized into three primary subsections. The first subsection describes the excitable medium design, which encompasses the neuronal model governing nodal dynamics, internodal connections, and the conditions required for the genesis of spiral waves. Subsequently, the tools employed to evaluate the propagation speed and the strength of the traveling wavefronts of spirals are introduced. Finally, the methodology for introducing inhomogeneity using the intrinsic parameters of the FHN neuronal model is discussed.

### 2.1. Excitable medium design

The FitzHugh–Nagumo (FHN) model is frequently employed to study the excitable dynamics of cardiac tissue and neuronal networks [43,44]. In the extended FHN model, a third variable representing the magnetic flux is incorporated. Since electrophysiological activities can produce a time-varying electromagnetic field, the effect of electromagnetic induction on the membrane potential must be considered [45,46]. In this study, the nodal dynamic is evolved by the three-variable memristive Fitzhugh–Nagumo model [47], whose kinetic form is as follows:

$$\begin{aligned}\dot{u}_{ij} &= -ku_{ij}(u_{ij}-a)(u_{ij}-1) - u_{ij}v_{ij} + k_0\rho(\varphi_{ij})u_{ij} + I_{ij}^{syn},\\ \dot{v}_{ij} &= \left(\varepsilon + \frac{v_{ij}\mu_1}{u_{ij}+\mu_2}\right)[-v_{ij} - ku_{ij}(u_{ij}-a-1)],\\ \dot{\varphi}_{ij} &= k_1u_{ij} - k_2\varphi_{ij}.\end{aligned} \tag{1}$$

For the node with the index $(i,j)$ on the lattice, $u_{ij}$ represents the transmembrane potential, $v_{ij}$ adjusts the variability of the slow current, and $\varphi_{ij}$ describes the magnetic flux. Frequently in the literature, a specific parametric set of $k=8$, $a=0.15$, $\mu_1=0.2$, and $\mu_2=0.3$ is chosen [47]. In the present work, we specifically focus on $\varepsilon$ parameter due to its modulatory effect on the medium's excitability. Thus, in the following sections, the numerical adjustment of the relaxation parameter $\varepsilon$ will be discussed in detail.

Fluctuations in the magnetic flux influence the membrane potential through a flux-controlled memristor, whose memductance is defined as:

$$\rho(\varphi_{ij}) = \frac{dq(\varphi_{ij})}{d\varphi_{ij}} = \alpha + 3\beta\varphi_{ij}^{\,2}, \tag{2}$$

where the memductance parameters are set as $\alpha = 0.2$ and $\beta = 0.3$. The parameters $k_1$ and $k_2$ represent electromagnetic induction gains, which are numerically set to $k_1 = 0.2$, and $k_2 = 1$. The Faradaic current produced by $\rho(\varphi)u$, modulates the membrane potential with a gain of $k_0 = 0.1$ [47].

Within the lattice structured by memristive FHN neurons, the internodal connections are facilitated by chemical synapses. The chemical coupling parametric setting allows us to generate desired spiral waves with distinct propagation speeds and wavefront strength. Assuming each node is connected to its eight nearest neighbors, the synaptic current introduced into the neuron's membrane at position $(i,j)$ is as follows:

$$\begin{aligned}I_{ij}^{syn} = & g_c\left(V_{rev}-u_{ij}\right)\times\\ & \Big[\Gamma\left(\lambda,\theta,u_{(i+1)j}\right)+\Gamma\left(\lambda,\theta,u_{(i-1)j}\right)+\Gamma\left(\lambda,\theta,u_{i(j+1)}\right)+\Gamma\left(\lambda,\theta,u_{i(j-1)}\right)+\\ & \frac{1}{2}\times\{\Gamma\left(\lambda,\theta,u_{(i+1)(j+1)}\right)+\Gamma\left(\lambda,\theta,u_{(i+1)(j-1)}\right)+\Gamma\left(\lambda,\theta,u_{(i-1)(j+1)}\right)\\ & +\Gamma\left(\lambda,\theta,u_{(i-1)(j-1)}\right)\}\Big],\end{aligned} \tag{3}$$

where $g_c$ denotes the intensity of the synaptic connection and $V_{rev}$ represents the reversal potential, indicating the voltage threshold where there is an equilibrium between inward and outward currents. The sign of $\left(V_{rev}-u_{ij}\right)$ determines the type of coupling, where if positive, the synapse is excitatory, and if negative, it is inhibitory. Concerning the range $0 \le u_{ij} < 1$, setting $V_{rev} = 2.5$ provides excitatory connections. Note that the synaptic connection between diagonal nodes is considered to be half as strong as that between axial ones. This distinction contributes to forming a finely shaped geometric spiral characterized by smoothly curved wavefronts.

The firing response of each neighboring synaptic terminal exhibits a threshold-like sigmoid behavior described as:

$$\Gamma(\lambda,\theta,u) = \frac{1}{1+e^{-\lambda(u-\theta)}}, \tag{4}$$

**Table 1**
Subsets of local arrays assigned with depolarized and repolarized initial values.

| | $u_0$ | $v_0$ | $\varphi_0$ |
|---|---|---|---|
| (1) | $(75:85, 1:100) = 2$ | $(75:85, 1:100) = 0$ | $(75:85, 1:100) = 0$ |
| (2) | $(86:105, 1:100) = 0.7$ | $(86:105, 1:100) = 0.2$ | $(86:105, 1:100) = 0.1$ |
| (3) | $(106:115, 1:100) = 0$ | $(106:115, 1:100) = 0.8$ | $(106:115, 1:100) = 0.2$ |

where $\lambda$ represents the slope of the sigmoid, and $\theta$ sets the firing threshold. This threshold establishes the operating point at which neurons respond smoothly, governed by the slope $\lambda$. Here, we set $\theta = 0.25$, a suitable response threshold for synaptic terminals. The remaining parameters related to chemical coupling, such as coupling strength $g_c$ and the sigmoidal activation slope $\lambda$, serve as control parameters, whose values will be further discussed.

This study examines a two-dimensional array consisting of 200 × 200 nodes. The Euler forward algorithm simulates the three-variable FHN model under no-flux boundary conditions. Given that the boundary is spatially open, any spiral locus that does not stabilize within the visible region generates waves that depart from the plane as they propagate outward. It is well understood that spiral waves arise from the interaction between depolarized and repolarized sites. This scenario is constructed through the setup of initial conditions. The entire lattice initially resides in a state of rest with $u_0 = v_0 = \varphi_0 = 0$. However, three subsets of local arrays are assigned different initial values, each encompassing depolarized and repolarized ensembles, and are defined in Table 1.

The configuration in Table 1 is essential for spiral wave generation. As the ensembles that initiate from a depolarized state commence firing, the opposing ensemble in a repolarized phase continues to excite the inactive neighboring nodes.

### 2.2. Estimating spiral wave propagation speed and wavefront strength

Through the help of chemical coupling parameters, especially $g_c$ and $\lambda$, we have identified three distinct cases in our study: (a) slow–weak, (b) fast–weak, and (c) fast–strong spiral waves. Note that "slow" and "fast" descriptors are relative terms specific to this research. The parameters associated with each scenario can be found in Table 2.

The propagation speed of a spiral is closely linked to the angular speed of its rotor, as the rotor is responsible for generating the circular propagating waves. When the spiral's rotor rotates at a slower speed, the produced wavefronts propagate with greater distances between them. Calculating the rotor's angular speed requires complex computations, which are beyond the scope of this study. Therefore, a suitable approach for understanding the speed of the spiral seed, or in general terms, the propagation speed of spiral wavefronts, is the duration between two sequential wavefronts reaching a fixed node within the lattice. Thus, one can analyze the spiking activity of a selected node. Note that we avoid nodes within the phase singularity region, where the sustained rotation of the spiral seed gives rise to the spiral pattern. Since many nodes start from rest due to the initial conditions, they become excitable upon the wavefront's arrival. Thus, the spiking period (namely $T_s$) of a node serves as a reliable measure of the wavefront's travel speed. Throughout the paper, we primarily analyze the signal $u_{(20,100)}(t)$, representing the voltage signal of a node situated outside the phase singularity region. Additionally, this node is not located within the local inhomogeneous zones we discuss later.

We apply a threshold filter to the lattice to determine the strength of the wavefronts. Consequently, the nodal spiking pattern transforms into a sequence of pulses. The duration of each pulse (namely $D_p$) represents the wavefront's intensity, indicating the total duration of the wave sensed by the node. The thresholding filter is applied as below:

$$\acute{u}_{(i,j)}(t) = \begin{cases} 1 & \text{if } u_{(i,j)}(t) \geq T, \\ 0 & \text{if } u_{(i,j)}(t) < T, \end{cases}$$

where $\acute{u}_{(i,j)}(t)$ is the nodal thresholded signal for any node $i, j \in [1, 200]$, and $T$ is the selected threshold. Based on our experiments, we propose $T = 0.7$, as the spiking pattern of the FHN model lies within the range $[0, 1)$. Setting $T < 0.7$ leaves the observed spiral pattern in the lattice intact. Conversely, $T \geq 0.7$ causes the traveling spiral wavefront to appear more constricted visually. Hence, $T = 0.7$ is an optimal threshold for distinguishing the active propagating wave from the silenced areas of the plane. Table 2 provides details on both the spiking periods $T_s$ and the durations of the pulses $D_p$ for the cases of slow–weak, fast–weak, and fast–strong spiral waves.

From a biological perspective, the terms mentioned can be interpreted in the context of the literature on the timings of action potentials in a myocyte. Here, 'pulse duration' refers to the action potential duration, 'spiking period' is synonymous with the diastolic interval, and their summation is termed the activation cycle length [13], also viewed as the refractory period. These analogies help elucidate the biological underpinnings of the work. However, we will proceed with our distinct parametric definitions based on our computational tool.

For each case, with an $\varepsilon = 0.005$, the spiking signal $u_{(20,100)}(t)$, and the pulse train resulted from the thresholding, $\acute{u}_{(20,100)}(t)$ are depicted in Fig. 1. For each spiral, the difference in propagation speed and wavefront strength can be sensed from the snapshots shown in Fig. 1. The slow–weak, fast–weak, and fast–strong spirals are illustrated in Fig. 1(a2), Fig. 1(b2), and Fig. 1(c2) respectively. The wavefronts of slow spirals traverse with more significant gaps between them. Moreover, the wavefronts of stronger spirals display increased thickness.

### 2.3. Medium inhomogeneity

In this paper, inhomogeneities arise due to parameter $\varepsilon$ mismatches between adjacent neurons. Before introducing the types of inhomogeneities examined in this study, we provide insights into the consequences of varying $\varepsilon$ values. We then analyze how these alterations influence a neuron's response based on the strength of the stimulus. The primary stimulus throughout this paper is the traveling spiral wave. However, in this subsection, we propose that $u_0$ can mimic the wavefront of the spiral wave as it reaches a specific node within the lattice. In other words, the initial condition can be perceived as an instantaneous stimulation at $t = 0$. Concerning the threshold $T = 0.7$, which signifies the minimum voltage for propagating wavefronts, we evaluate the responses of a single FHN neuron to conditions $u_0 = 0.2$, $u_0 = 0.7$, and $u_0 = 1.2$. This evaluation enriches our comprehension of how slow–weak, fast–weak, and fast–strong spiral waves influence nodal responses. Additionally, in line with the findings presented in the subsequent sections, this analysis illuminates the reasons behind the robustness of spiral wave propagation against specific inhomogeneity ranges and its vulnerability in others.

In Fig. 2, the membrane potential response of a single FHN neuron is displayed for different values of $\varepsilon = 0$, 0.0025, 0.005, 0.0075, 0.01, 0.03, 0.1 and 0.5. In Fig. 2(a) for $(u_0, v_0, \varphi_0) = (0.2, 0.2, 0.1)$ the response is damping. When $\varepsilon$ values are low, specifically $\varepsilon < 0.1$, the response is underdamped, with a notable overshoot as we set $\varepsilon = 0$. When the neuron has $\varepsilon = 0.5$, the overshoot is not pronounced, indicating a more overdamped response. In Fig. 2(b) with $(u_0, v_0, \varphi_0) = (0.7, 0.2, 0.1)$ the response is also damping. Interestingly, even a high value of $\varepsilon = 0.5$, results in an underdamped response. Nevertheless, the time constant for these responses varies significantly. A smaller $\varepsilon$ corresponds to a higher time constant, leading to a more prolonged plateau. In such cases,

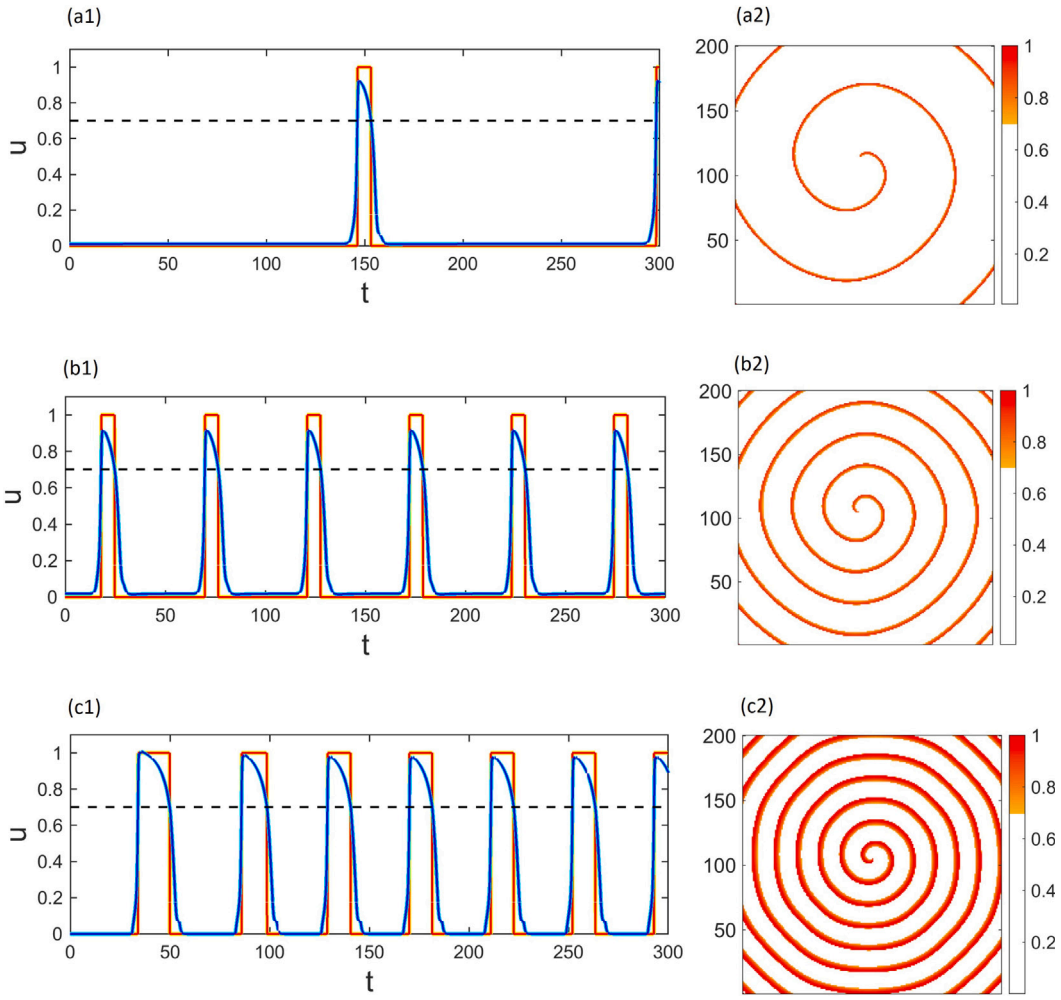


**Fig. 1.** Spiral waves with varying wavefronts propagation speed and strength. The relaxation parameter is $\epsilon = 0.005$. In the left column, the spiking signal $u_{(20,100)}(t)$ is displayed in blue in the foreground. The pulse train in the background with the orange coloring features the thresholded signal $\acute{u}_{(20,100)}(t)$. A black dotted line represents the threshold $T = 0.7$ that converts the blue spiking signal into the orange pulse train. The period of spiking at the nodal index $(20, 100)$ serves as an estimate for the propagation speed. The strength of the wavefront is deduced by the pulse train, where the duration of each pulse indicates the wavefront's strength. In the right column, the whole lattice is displayed, and the corresponding thresholded spiral wave for each scenario is depicted as follows: (a) slow–weak, (b) fast–weak, and (c) fast–strong. In case (a) the propagation speed and strength of wavefronts are the lowest. Conversely, case (c) exhibits a spiral wave with a higher speed of propagation and stronger wavefronts.

**Table 2**
Parametric setting of generated spiral waves, the spiking period, and the pulse duration values computed by $u_{(20,100)}(t)$ representing the speed and strength of spiral wavefronts depicted in Fig. 1 respectively.

| Type of spiral wave | Chemical coupling setting | Spiking period | Pulse duration |
|---|---|---|---|
| | $g_c$ - $\lambda$ | $T_s$ | $D_p$ |
| (a) Slow–weak | 0.02 - 12 | 155 s | 6 s |
| (b) Fast–weak | 0.025 - 12 | 50 s | 6 s |
| (c) Fast–strong | 0.025 - 50 | 40 s | 10 s |

the FHN neuron maintains its excited state for an extended duration. This behavior is typical of systems with inadequate damping, where excitation is not dissipated quickly. Setting higher values of $\epsilon$ leads to the faster dissipation of neuron excitation. Finally, in Fig. 2(c) we set $(u_0, v_0, \varphi_0) = (1.2, 0.2, 0.1)$. In these conditions, all responses are overdamped. The neuron returns to equilibrium smoothly, without any overshoot. However, the plateau behavior is maintained. Besides the information in Fig. 2, it is essential to note that any $u_0 < 0.2$ results in an identical overdamped response, regardless of the $\epsilon$ value chosen.

Given this study, as the rotating spiral voltage predominantly falls within $0.7 < u < 1$, the scenarios in Fig. 2(b) are most relevant, representing the response of a neuron in the lattice as the wave hits its location.

Inhomogeneity can be distributed in two primary ways: random or uniform. Additionally, the inhomogeneity zone can be global, covering the entire lattice, or local, confined to a particular region. In this study, we examine three distinct scenarios:

1. Globally distributed random inhomogeneity
2. Locally distributed random inhomogeneity
3. Locally distributed uniform inhomogeneity

In every scenario, the default value of $\epsilon$ is set at 0.005 unless stated otherwise. Our primary objective is to elevate the value of $\epsilon$, randomly or uniformly, within the planar arrays. This is to assess the robustness of different spirals, including slow–weak, fast–weak, and fast–strong, against these inhomogeneities. Consequently, for each

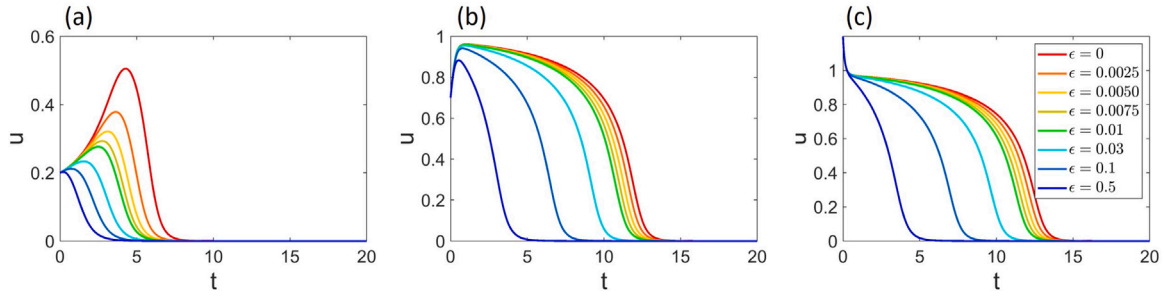


**Fig. 2.** The membrane potential response of a single FHN neuron, $u(t)$, for different values of $\varepsilon$ = 0, 0.0025, 0.005, 0.0075, 0.01, 0.03, 0.1 and 0.5. (a) With initials $(u_0, v_0, \varphi_0) = (0.2, 0.2, 0.1)$, responses are underdamped. The maximum overshoot belongs to $\varepsilon = 0$. (b) With $(u_0, v_0, \varphi_0) = (0.7, 0.2, 0.1)$, responses are underdamped with conserved excitation in the form of a plateau. The most prolonged plateau belongs to $\varepsilon = 0$. (c) With $(u_0, v_0, \varphi_0) = (1.2, 0.2, 0.1)$, responses are overdamped with the same plateau patterns as in (b). The responses indicate that as the value of relaxation parameter in the FHN model is increased, the neuron's capacity to maintain an excited state diminishes.

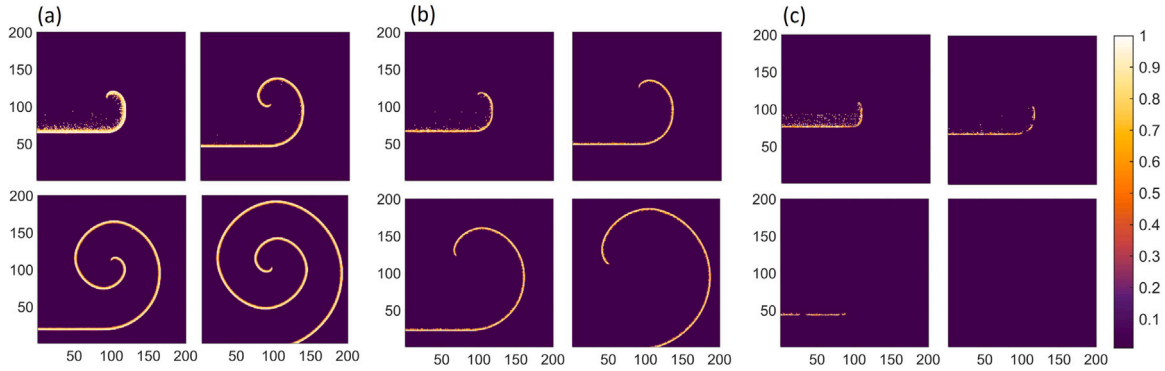


**Fig. 3.** Evolution of the slow–weak spiral wave in a lattice with globally distributed random inhomogeneity. For each case, the inhomogeneity interval is taken as (a) $\varepsilon \in [0, 0.01]$, (b) $\varepsilon \in [0, 0.05]$, (c) $\varepsilon \in [0, 0.1]$. The wave's reentrant capability is intactly maintained in case (a). In case (b) the spiral rotor succeeds to form, however the wavefronts are weakened due to the total elevation in the $\varepsilon$ value. In case (c), when $\varepsilon_{max} = 0.1$, an increased number of nodes randomly become less excitable. The reduction in the total excitability of the plane causes spiral rotors to become unstable and eventually cease.

scenario, we report the maximum tolerable value of $\varepsilon$ for the spiral rotor. This approach stems from the observation that increasing $\varepsilon$ results in diminished responses with a reduced capacity to maintain excitation or plateau behavior.

## 3. Results

### 3.1. Globally distributed random inhomogeneity

In this section, we evaluate the formation of spiral waves within a lattice of FHN neurons. For these neurons, the $\varepsilon$ parameter is randomly chosen from the interval $[0, \varepsilon_{\max}]$. Here, $\varepsilon_{\max}$ represents the maximum tolerable inhomogeneity. For each scenario – slow–weak, fast–weak, and fast–strong – $\varepsilon_{\max}$ is increased in three stages, as depicted in subplots (a) to (c) in Figs. 3 to 5. Each subplot displays a series of snapshots illustrating the temporal evolution of spirals within the 2D plane.

Initially, for all of the cases, we set $\varepsilon_{\max} = 0.01$. The subsequent two values for $\varepsilon_{\max}$ vary depending on the type of spiral. The second value represents a mid-range point where the spiral locus stabilizes. However, during this phase, the characteristics of the spiral, such as propagation speed and wavefront strength, are diminished. In the final scenario, $\varepsilon_{\max}$ is adjusted to the lowest value at which spirals can no longer form. In this situation, the free end of the spiral wave, which would typically form a stable rotor, fails to reenter itself at a fixed spatial zone and instead moves outward, eliminating any propagating wave from the lattice. For each scenario, we also report the maximum tolerable $\varepsilon$ value if all neurons in the lattice had that value uniformly. As anticipated, $\varepsilon_{\max}$ in the random configuration is higher than the uniform $\varepsilon$ value.

In Fig. 3, we adjust the chemical coupling parametric settings to generate a slow–weak spiral. In Fig. 3(a), the inhomogeneity parameter $\varepsilon$ is randomly selected from the interval $\varepsilon \in [0, 0.01]$. As interactions between locally excited sites and the silent lattice occur, the free end of the vertically propagating wave bends, reentering inwards. Consequently, a stable rotor forms, completing the spiral pattern. This suggests that the slow–weak spiral can withstand a random inhomogeneity with a maximum value of $\varepsilon = 0.01$. In Fig. 3(b), the interval of inhomogeneity is broadened to $\varepsilon \in [0, 0.05]$. Under this condition, a traveling spiral pattern dominates the plane through further inward rotation. However, the original shape and dynamics of the spiral are affected. The propagation speed reduces, causing the circular wavefronts to move in higher proximity. Examining the snapshots in Fig. 3(b) more closely, we observe that the spiral rotor does not remain stationary at a specific node but meanders along a circular path, confined to an area encompassing several nodes. Such a meandering spiral wave arises from a destabilization source. Therefore, introducing a higher degree of inhomogeneity, taking $\varepsilon_{\max} = 0.05$, destabilizes the stationary rotor, though not to the extent of immediate elimination after temporal evolution starts. In Fig. 3(c), $\varepsilon_{\max}$ slightly surpasses the maximum tolerable value for spiral rotors to endure. With random inhomogeneity in the range $\varepsilon \in [0, 0.1]$, the formation of the spiral rotor, given the selected initial condition, fails, disrupting the reentrant-free end of the traveling wave. The residual plane wave quickly exits the observable region in the initial iterations. Therefore, the formation of a slow–fast spiral ceases at $\varepsilon_{\max} = 0.1$. Interestingly, this value surpasses the maximum $\varepsilon$ if uniformly set throughout the lattice. Based on our experiments, if the $\varepsilon$ parameter is globally set at $\varepsilon = 0.05$, the formation of such a spiral does not occur.

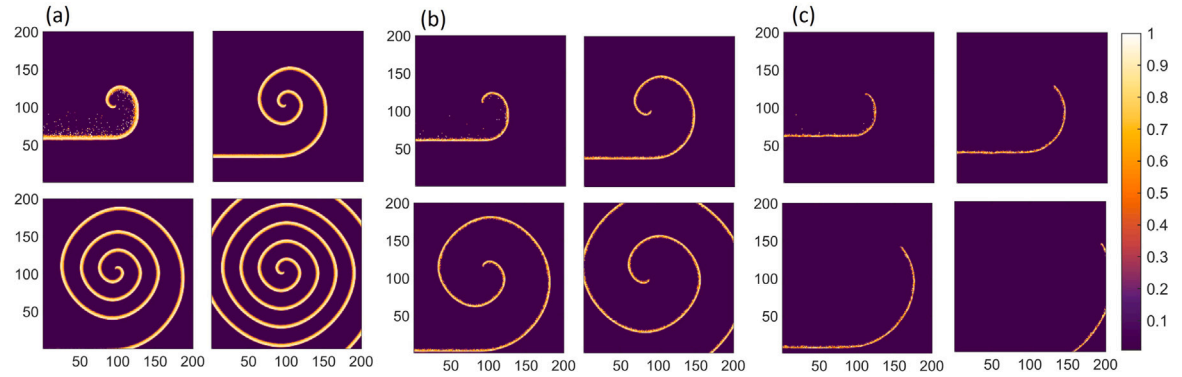


**Fig. 4.** Evolution of the fast–weak spiral wave in a lattice with globally distributed random inhomogeneity. For each case, the inhomogeneity interval is taken as (a) $\varepsilon \in [0, 0.01]$, (b) $\varepsilon \in [0, 0.1]$, (c) $\varepsilon \in [0, 0.18]$. The wave's reentrant capability of spiral tip maintained in case (a). In case (b) the spiral rotor succeeds to form, however the wavefronts are weakened due to the random decrease in excitability of neurons. In case (c), where $\varepsilon_{\max} = 0.18$, the lattice does not tolerate the diminished excitability, leading to the failure of the fast–weak spiral rotor to become spatially stable.

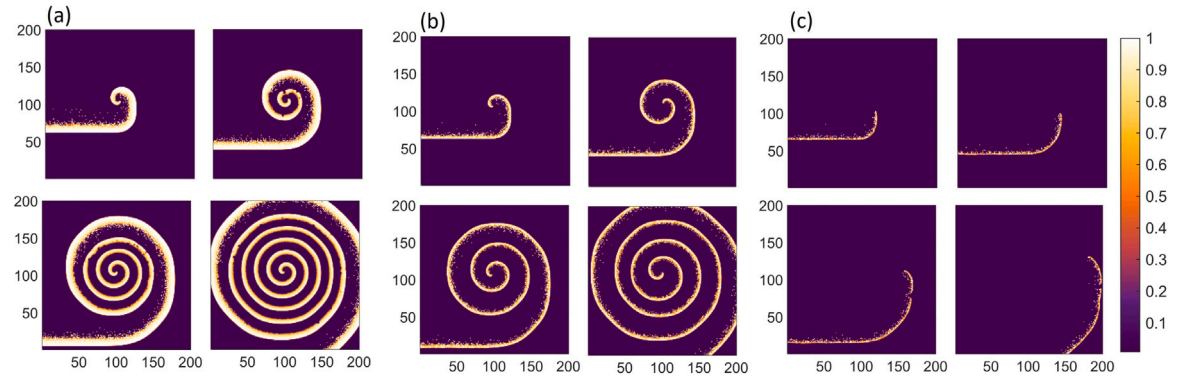


**Fig. 5.** Evolution of the fast–strong spiral wave in a lattice with globally distributed random inhomogeneity. For each case, the inhomogeneity interval is taken as (a) $\varepsilon \in [0, 0.01]$, (b) $\varepsilon \in [0, 0.1]$, (c) $\varepsilon \in [0, 0.25]$. In cases (a) and (b), where $\varepsilon_{\max}$ of random inhomogeneity is less, the rotor of the fast–strong spiral survives. Few scattered excited nodes can be observed near the traveling wavefronts, as the lattice synaptic connection is enhanced in the case of fast–strong spiral wave. In case (c) even a medium synaptically suitable for the generation of a fast–strong spiral wave does not tolerate the diminished excitability at $\varepsilon_{\max} = 0.25$. The total reduction in the medium excitability caused by $\varepsilon$ increase leads to the failure of the fast–strong spiral rotor to form.

In Fig. 4, the chemical coupling parametric settings are adjusted to generate a fast–weak spiral. Specifically, in Fig. 4(a), the inhomogeneity parameter $\varepsilon$ is randomly selected from the interval $\varepsilon \in [0, 0.01]$. The selected initial condition successfully leads to the formation of a well-shaped fast–weak spiral. A random inhomogeneity with a maximum value of $\varepsilon = 0.01$ is tolerable, maintaining the characteristics of the spiral. In contrast, extending the inhomogeneity range to $\varepsilon \in [0, 0.1]$ results in a decreased propagation speed, as shown by the increased distance between sequential wavefronts and diminished strength. Notably, within this range, the slow–weak spiral was eliminated, as seen in Fig. 3(c). For the fast–weak spiral to lose its reentrance capability, inhomogeneity must be expanded to $\varepsilon \in [0, 0.18]$, as illustrated in Fig. 4(c). Here, the spiral tip's inability to complete a rotation leads to its translational movement out of the lattice. Experiments suggest that if $\varepsilon$ is uniformly set at $\varepsilon = 0.07$, the spiral does not form, indicating that the maximum tolerable $\varepsilon$ in a random distribution is higher, at $\varepsilon_{\max} = 0.18$.

In the final scenario, a fast–strong spiral is analyzed. As depicted in Fig. 5(a), the inhomogeneity range is set to $\varepsilon \in [0, 0.01]$. Initially, the wavefront that forms is notably stronger but subsequently reverts to the strength expected from the fast–strong spiral. Upon closer inspection, it becomes evident that the initial wavefronts are encircled by scattered excited nodes, which do not align cohesively to form a consistent wavefront. Given that the range $\varepsilon \in [0, 0.01]$ represents a domain where neurons are highly excitable, nodes not directly part of the main wavefront can demonstrate excited behaviors. Nonetheless, this phenomenon is more pronounced in the context of the fast–strong spiral, where chemical coupling parameters are more suitable for wave propagation. In Fig. 5(b), extending the inhomogeneity range to $\varepsilon \in [0, 0.1]$ results in a weakened spiral, both in terms of wavefront strength and propagation speed. Ultimately, taking $\varepsilon_{\max} = 0.25$, the spiral wave formation becomes unachievable, as displayed in Fig. 5(c). The wave tip no longer exhibits reentrancy and drifts out of the observable region. If $\varepsilon$ value had been uniformly set, the spiral could tolerate a value up to 0.11 in this scenario.

After discussing these results, examining the response types in Fig. 2(b) is worthwhile. When stimulated under this condition, neurons exhibit an underdamped response, resulting in an overshoot. This allows the excited neuron to maintain its excitation for an extended duration. Such a capability is advantageous when discussing wave propagation in a coupled lattice, as neurons retain sufficient time to transfer excitement to neighboring neurons. Particularly when a plateau arises, the excitation persists even longer. However, as $\varepsilon$ value increases, the neuron's capacity to stay depolarized decreases. For a lattice with a uniform higher value of $\varepsilon$, the outcomes are more straightforward to comprehend. Globally, the entire plane becomes less excitable, thus no spiral pattern is shaped. Yet, when neighboring neurons exhibit varying abilities, as we set $\varepsilon$ values randomly, the situation becomes more complicated.

By randomly selecting the $\varepsilon$ value, which results in variable excitability within the medium, it is the lattice's collective behavior, rather than the properties of a single neuron, that is examined. Our findings from Figs. 3 to 5 demonstrate that more excitable neurons can compensate for less excitable ones, sustaining the spiral wave pattern

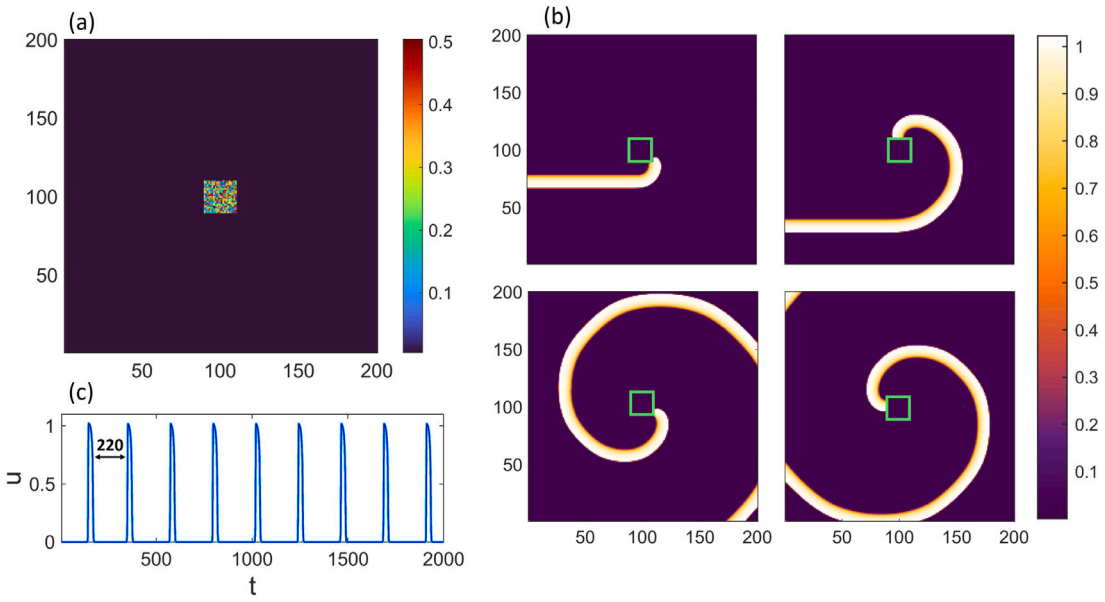


**Fig. 6.** Local-centered inhomogeneity constructed of 20 × 20 nodes. (a) The nodal $\epsilon$ distribution within the lattice. The inhomogeneous site is created by random values of $\epsilon \in [0, 0.5]$. The rest of the lattice has a consistent value of $\epsilon = 0.005$. (b) Snapshots of the formation of a fast–strong spiral, with its tip pinned to the inhomogeneous zone. This spiral wave rotates around the periphery of the inhomogeneous square. Due to the longer trajectory the spiral rotor has to navigate to complete a 360-degree rotation, the number of propagating wavefronts within the lattice is reduced, leading to a decreased propagation speed. (c) The spiking pattern of $u_{(20,100)}(t)$, representing the propagation speed of the spiral wave. The spiking period is notably increased to $T_s = 220$.

across the plane. However, this compensatory ability has its limits. The functionality of an excessively unexcitable neuron (with a high $\epsilon$ value) cannot be compensated for, making the pattern formation unattainable. Our findings indicate that setting $\epsilon_{\max} = 0.1, 0.18$, and 0.25, for slow–weak, fast–weak, and fast–strong spiral waves, respectively, reduces the total excitability of the medium, and this deficiency cannot be compensated.

### 3.2. Locally distributed random inhomogeneity

In this section, instead of a global distribution, we introduce inhomogeneity within a specified region, namely locally distributed. Biologically, when such conditions are localized, these zones can be perceived as conduction barriers, either non-conductive or semi-conductive, as studied in vitro [48]. The chemical coupling parameter is set to generate a fast–strong spiral wave. Based on observations from the previous section, this spiral demonstrated remarkable resilience against medium inhomogeneity, tolerating $\epsilon_{\max} = 0.25$. Nodes outside the localized inhomogeneity are assigned a value of $\epsilon = 0.005$. Within the inhomogeneous zone, $\epsilon$ is randomly taken from the range $[0, 0.5]$. Note that the chosen $\epsilon_{\max} = 0.5$ surpasses the previously identified threshold for the fast–strong spiral when inhomogeneity was distributed globally. The placement of this local inhomogeneity can vary; however, we specifically focus on where the spiral rotor is likely to appear. This is because the rotor, or phase singularity, is essential for the reentrance and sustained propagation of the spiral wave. The rotor forms around the coordinates $(100, 100)$ based on the selected initial conditions. Consequently, the locally inhomogeneous region is designed as a symmetrical square centered at node $(100, 100)$. We consider three scenarios varying in the size of this inhomogeneous square: dimensions of $20\times20, 40\times40$, and $80\times80$ are explored. The outcomes of these configurations present notable differences compared to cases with globally distributed inhomogeneity.

Fig. 6(a) represents the results for a local inhomogeneous area of size 20 × 20, where the inhomogeneity is randomly distributed in the range $\epsilon \in [0, 0.5]$. As the fast–strong spiral wave attempts to form by its free-end reentrance, it tends to rotate around the inhomogeneous zone. Surprisingly, although the spiral wave tip cannot enter the inhomogeneity site, it does not prevent the formation of the spiral locus. Instead, it becomes the center of the wave tip's rotational movement. The snapshots in Fig. 6(b) exhibit the rotational movement of the generated spiral wave, making a complete turn around the inhomogeneous square's periphery. However, in a homogeneous lattice with $\epsilon = 0.005$, the spiral seed takes localized rotations, restricted to a point, as shown in Fig. 1(c2). Based on the spiking period of $u_{(20,100)}(t)$ in Table 2, the propagation period of fast–strong spiral is estimated by spiking period $T_s = 40$. Conversely, in this scenario, the spiral tip moves rotationally along a trajectory composed of several nodes. Therefore, the time taken for the spiral to turn on the margin of the inhomogeneity site affects the propagation speed of its wavefronts. Fig. 6(c) represents the spiking pattern of $u_{(20,100)}(t)$, suggests that the spiking period has increased to $T_s = 220$, indicating the decelerated propagation of spiral wavefronts. It is important to note that since the main body of the spiral remains within the lattice of $\epsilon = 0.005$, the strength of the wavefronts remains unchanged, as initially seen in Fig. 1(c2).

Fig. 7(a) displays results for a local inhomogeneous area expanded to a size of 40 × 40. When the fast–strong spiral wave's tip attempts to reenter itself, it pins to the inhomogeneous zone. Similar to previous observations, the spiral wave tip cannot penetrate the inhomogeneity site, essentially becoming the focal point of the wave tip's rotational movement. Snapshots shown in Fig. 7(b) capture the rotational movement of the produced spiral wave. Its tip, pinned to the inhomogeneity, orbits the inhomogeneous perimeter. Due to the larger periphery of the 40 × 40 localized inhomogeneity, the spiral tip navigates a more extended path to complete a 360-degree rotation. Consequently, the observable region depicts a contracted spiral body, and there is an elongation in the propagation period of the circular wavefronts. This observation is further proved by Fig. 7(c), which illustrates the spiking pattern of $u_{(20,100)}(t)$. The spiking period has stretched to $T_s = 400$, indicating the decelerated propagation pace of spiral wavefronts. As previously highlighted, the spiral pattern body lies within the lattice where $\epsilon = 0.005$, keeping the strength of the wavefronts consistent.

In the last scenario, the inhomogeneity size is increased, spanning a square of 80 × 80 nodes. The nodal distribution of $\epsilon$ within the lattice is portrayed in Fig. 8(a). Snapshots in Fig. 8(b) demonstrate spiral wave

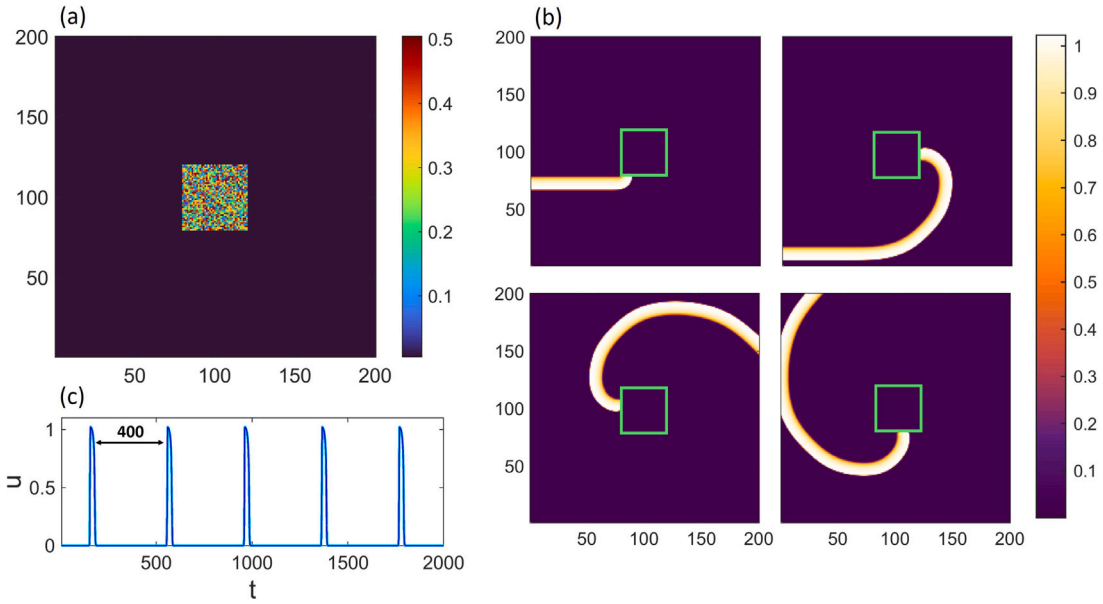


**Fig. 7.** Local-centered inhomogeneity constructed of 40 × 40 nodes. (a) The nodal $\epsilon$ distribution within the lattice. The inhomogeneous site is created by random values of $\epsilon \in [0, 0.5]$. The rest of the lattice has $\epsilon = 0.005$. (b) Snapshots of the formation of a fast–strong spiral, with its tip pinned to the inhomogeneous zone. This spiral wave rotates around the periphery of the inhomogeneous square. Because of the longer trajectory the spiral rotor must navigate to complete a 360-degree rotation, the spiral body within the observable region appears shrunken. The decrease in the tip curvature of spiral results in loosely shaped circular wavefronts. (c) The spiking pattern of $u_{(20,100)}(t)$, representing the propagation speed of the spiral wave. The excitement period is notably increased to $T_s = 400$.

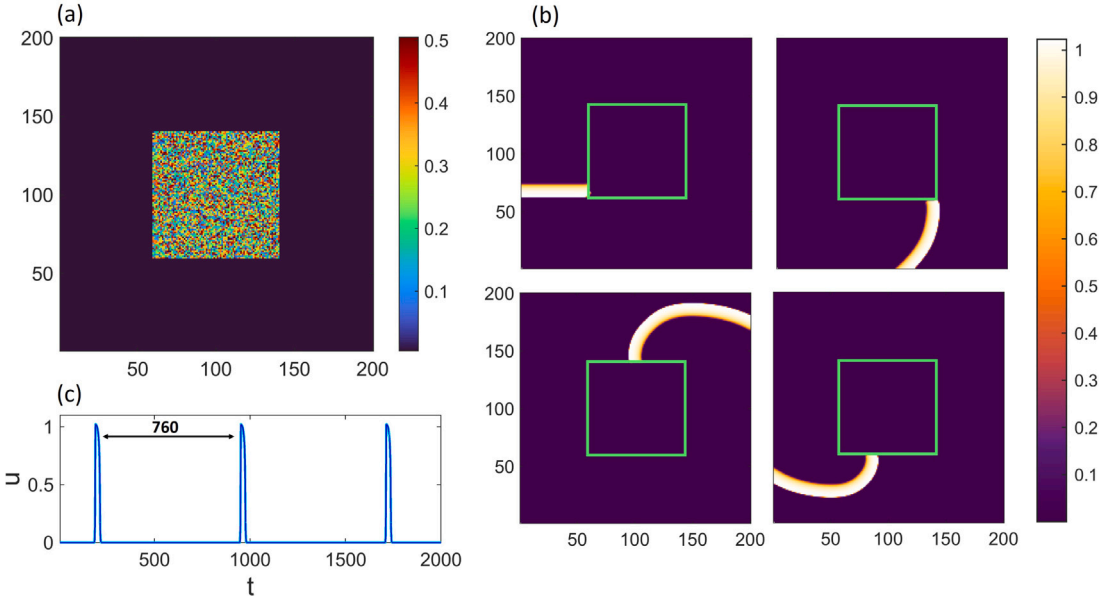


**Fig. 8.** Local-centered inhomogeneity constructed of 80 × 80 nodes. (a) Inhomogeneity parameter $\epsilon$ distribution within the lattice. Random values of $\epsilon$ within the range $[0, 0.5]$ characterize the inhomogeneous site. Outside of the inhomogeneous region $\epsilon = 0.005$. (b) Snapshots of the formation of a fast–strong spiral, with its tip anchored to the inhomogeneous zone. This spiral wave orbits the periphery of the inhomogeneous square. Due to the extended periphery of the inhomogeneity zone, the spiral rotor has to navigate a longer path, and even a more minor part of the spiral body is present within the observable region. (c) The spiking pattern of $u_{(20,100)}(t)$, an indicator of the spiral wave's propagation speed. The period of excitement is increased to $T_s = 760$.

formation in which the previous scenarios can be observed. First, the spiral tip is pinned to the inhomogeneous zone. Then, this anchored tip orbits the inhomogeneity's periphery. Given the 200 × 200 dimensions of the entire lattice, the local inhomogeneous zone of 80 × 80 is notably large. As the spiral tip is bound to pave this extensive path, even a more limited part of the spiral body is present within the observable area. Consequently, the propagation speed for the spiral wavefront is decelerated. As displayed in Fig. 8(c), the spiking pattern of $u_{(20,100)}(t)$ manifests a period of $T_s = 760$, consistent with the reduced propagation velocity of the traveling spiral within the lattice. As before, the intensity of the wavefronts remains unaltered.

The results presented in Figs. 6 to 8 highlight several vital insights. First, when a spiral forms within a medium containing a random, concentrated inhomogeneity spot, the tip of the spiral cannot enter this spot. Nevertheless, direct contact between the spiral rotor—which acts as the primary source of the spiral wave propagation—does not result in the complete elimination of the spiral wave. The spiral pattern can maintain its integrity and consistency if the remainder of the spiral body is within a properly excitable medium (as the rest of the

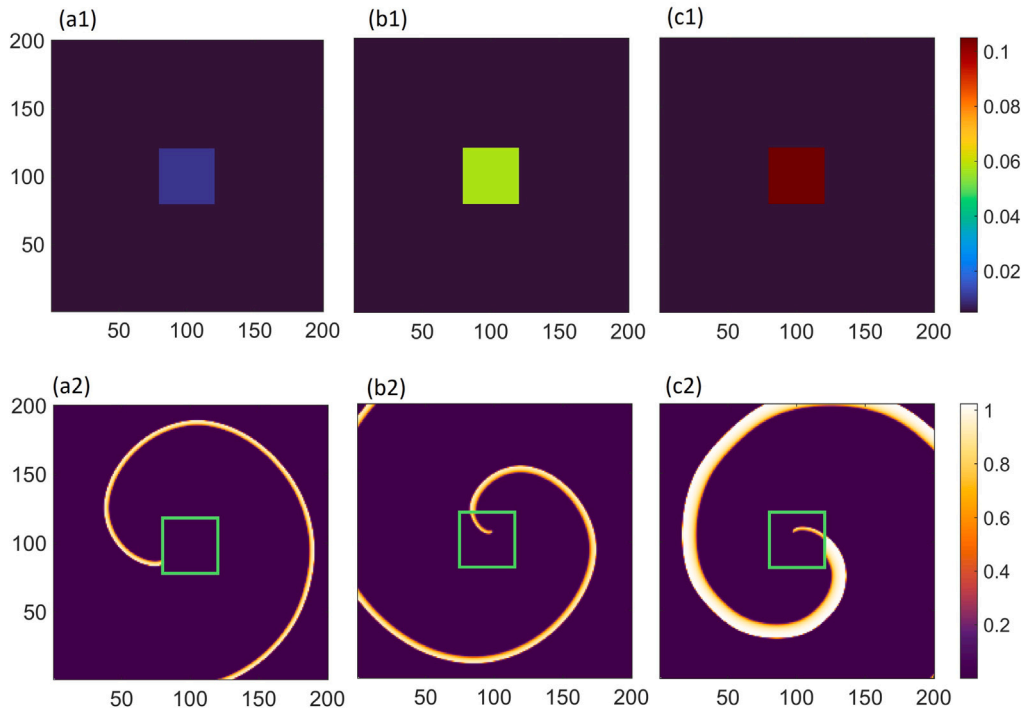


**Fig. 9.** A local-centered inhomogeneity with a uniform distribution constructed of 40 × 40 nodes. Outside of the inhomogeneous region, $\epsilon = 0.005$. The first row displays the $\epsilon$ distribution within the lattice. The inhomogeneity $\epsilon$ for each case is: (a1) $\epsilon = 0.01$, (b1) $\epsilon = 0.055$, (c1) $\epsilon = 0.1$. The interaction of spiral waves with the induced inhomogeneity is depicted in the second row with: (a2) slow–weak, (b2) fast–weak, (c2) fast–strong spiral wave. In case (a), the slow–weak spiral tip is unable to penetrate the inhomogeneity site with $\epsilon = 0.01$. Consequently, the spiral cannot maintain its nodal locus rotation and rotates around the periphery of the inhomogeneity, essentially becoming anchored to it. In case (b), the fast–weak spiral exhibits stronger wavefronts, enabling it to penetrate an inhomogeneity site with $\epsilon = 0.055$, which allows the spiral to preserve its nodal locus rotation. In case (c), with a fast–strong spiral, maintaining the nodal locus rotation is achievable even at a higher inhomogeneity value of $\epsilon = 0.1$. Note that for cases (b) and (c) the nodal loci are preserved at the cost of a weakened wavefront within the inhomogeneous site.

lattice is homogeneous with $\epsilon = 0.005$). Secondly, the localized inhomogeneity becomes the center around which the spiral's tip rotates. Throughout its rotation, the spiral tip remains continuously pinned to the inhomogeneity. This continuous attachment causes the spiral rotor to meander along the inhomogeneity's perimeter. As the size of the inhomogeneity increases, so does its periphery, meaning the anchored spiral tip must navigate an extended path. For the spiral wave to generate a propagating circular wavefront, the spiral tip has to complete a 360-degree rotational reentrance. Consequently, the longer the meandering trajectory, the larger the radius of rotation becomes, increasing the curvature of the spiral wave. Within the observable area of the lattice, a smaller portion of the spiral becomes evident.

To conclude, when evaluating the robustness of the spiral wave against a localized inhomogeneity with a random distribution, the spiral wave proves robustness. Its tip survives by being anchored onto the inhomogeneity and maintaining its self-sustained rotation.

### 3.3. Locally distributed uniform inhomogeneity

In this section, we evaluate the interactions of three types of spiral waves – slow–weak, fast–weak, and fast–strong – with a local inhomogeneity site where the $\epsilon$ value is uniformly set. The excitability of the rest of the lattice is defined by $\epsilon = 0.005$. As previously noted, the random inhomogeneity site acts as the pivot for the spiral wave's rotation due to the attachment of its tip, which never penetrates this site. Our primary goal is to determine the maximum $\epsilon$ value within the uniform inhomogeneity zone that permits the spiral tip's entry while maintaining its intended nodal locus. By 'nodal locus,' we refer to an intrinsic characteristic of a spiral wave in which its rotor remains stationary and is bound to a specific site, known as the phase singularity. Given the distinct characteristics of the three spirals, the $\epsilon_{max}$ value varies for each. Within the forthcoming results, the inhomogeneity site is a square of 40 × 40 size.

Fig. 9(a1) demonstrates that the inhomogeneity value is set to $\epsilon = 0.01$, implying that compared to the rest of the lattice, $\epsilon$ is doubled. The manifestation of the spiral wave with this inhomogeneity is illustrated in Fig. 9(a2). The spiral tip cannot enter such an inhomogeneity. Although our primary goal was to determine the maximum $\epsilon$ value that allows the spiral tip to penetrate, we made an exception for the slow–weak spiral. Our experiments suggest that setting the local inhomogeneity to $\epsilon < 0.01$ allows the entrance of the spiral tip, notably, with no change in the spiral wave geometry. The slow–weak spiral seemingly lacks the strength to enter an inhomogeneity site with high $\epsilon$ without compromising consistency. This observation becomes clearer when evaluating the subsequent scenarios. In Fig. 9(b1), the local inhomogeneity is set to $\epsilon = 0.055$. By introducing a fast–weak spiral within this lattice, the spiral tip manages to penetrate the inhomogeneity site, albeit with difficulty. The segment of the spiral wave within the inhomogeneity weakens, as portrayed in Fig. 9(b2). For $\epsilon < 0.055$, the spiral tip's degradation is not as pronounced, while for $\epsilon > 0.055$, the inhomogeneity blocks the spiral tip's entrance. Therefore, the upper limit of $\epsilon$ that permits the entry of the spiral tip while retaining its nodal locus, in this instance, is $\epsilon = 0.055$. Such an outcome suggests that the fast–weak spiral case is more robust and tends to maintain its nodal locus, even within the boundaries of an inhomogeneity zone where node excitability is diminished due to increased $\epsilon$ values. Lastly, the inhomogeneity value is set at $\epsilon = 0.1$, as displayed in Fig. 9(c1). This inhomogeneity value accommodates the fast–strong spiral wave, allowing it to access the inhomogeneity zone while preserving its nodal locus, as shown in Fig. 9(c2). This entry, however, comes at the cost of diminished strength of the penetrated portion of the spiral tip. Setting $\epsilon > 0.1$ causes the spiral rotor to become nonstationary, meandering around the periphery of the inhomogeneous zone.

## 4. Discussion

The manifestations seen from locally distributed inhomogeneities lead us to perceive them as obstacles. Yet, it is essential to understand that these inhomogeneities do not strictly qualify as anatomical obstacles. They are made up of excitable cells with excitability that varies from their neighboring regions, classifying them as functional inhomogeneities. In contrast, obstacles, being naturally occurring structural inhomogeneities like arteries, can anchor a drifting spiral wave and stabilize it [49]. Nevertheless, the anchoring phenomenon observed in our case of local inhomogeneity aligns consistently with that caused by anatomical obstacles.

Existing literature investigates the reasons behind the attachment of reentrant seeds to anatomic obstacles. Related to wave conduction or blockage, the term "safety factor" is defined [50]. This factor is determined by the relationship between the available current to excite cells (source) at the wavefront and the required depolarizing current for adjacent cells to reach the excitation threshold (sink). This relationship dictates whether conduction will occur or be blocked [51]. Based on the source–sink ratio, the safety margin for wave propagation provides insights into the pinning phenomenon. It is important to note that not all segments of a spiral wavefront possess the same stimulating efficacy (source). Due to its high curvature, the tip of a spiral wave inherently has a lower safety margin (source) for propagation compared to the less curved periphery of the wavefront. When faced with a relatively larger obstacle, the sink of a rotating wavefront diminishes, leading to an increased source-to-sink ratio (safety factor). This amplification in the safety factor engages a larger domain of cells. As a result, all cells at the boundary of the obstacle become depolarized. This collective depolarization at the obstacle's boundary facilitates the attachment of the spiral seed to the obstacle, elucidating the anchoring mechanism [34].

## 5. Conclusion

The present report constructed a lattice of chemically coupled memristive FitzHugh–Nagumo neurons. The initial condition and the chemical coupling setting were adjusted to produce three cases of spirals, varying in propagation speed and wavefront strength. Tools for assessing the mentioned characteristics were introduced. The relaxation parameter was employed as the source of functional inhomogeneity, whose variation produced different responses from sustained depolarization to becoming rapidly damped. Both global and local spatial inhomogeneities were examined. Global inhomogeneity distributed stochastically was assessed, and the resilience of emerging spirals to variations in the range of such distribution was also evaluated. For the case of local inhomogeneity, we examined how the spiral tip could penetrate. Two types of local inhomogeneities were studied: one with random excitability-tuning parameters and another with a uniform distribution. When pinning was observed, its secondary effects on propagation speed were further analyzed.

In the case of global inhomogeneity, the relaxation parameter was randomly chosen within a region that ranged from zero to a maximum value. Low values were observed to enable an excited neuron to sustain its excitation for a prolonged period, providing an advantage for wave propagation. By randomly increasing the range's maximum value, neurons with diminished ability to remain depolarized were generated. Consequently, the entire plane was rendered less excitable on a global scale. Our findings demonstrated that more excitable neurons could compensate for those less excitable, maintaining the spiral wave pattern across the plane. However, this compensatory capability was found to have boundaries. In all spiral waves, whether slow–weak, fast–weak, or fast–strong, setting a specific maximum resulted in neurons so rapidly damped that this deficiency could not be compensated for. Thus, the emerging spiral wave was broken or driven out of the lattice.

In the case of local inhomogeneity, two distinct scenarios were observed, depending on whether the inhomogeneity distribution was random or uniform. In the random scenario, it was noted that the spiral tip could not penetrate the inhomogeneous spot. However, the emerging spiral wave remained resilient against this inhomogeneity, even if the inhomogeneous spot was situated at the location where the spiral rotor would eventually interact with it. Nonetheless, the spiral tip was consistently anchored to the inhomogeneity during its rotational movement, meandering around the inhomogeneity periphery. The spiral tip had to complete a 360-degree rotational reentry to generate a propagating circular wavefront. Thus, as the meandering path lengthened owing to the increased size of the inhomogeneous spot, the curvature of the spiral tip was found to decrease, as did the propagation speed of the circular wavefronts.

In the latter scenario, where the local inhomogeneous spot had a uniform relaxation parameter, findings emphasized that not every type of inhomogeneity led to the anchoring and meandering of the spiral wave. Certain inhomogeneities were penetrable, analogous to semi-conduction barriers in heart tissue, and the nodal locus of the spiral rotor remained undisturbed.

## CRediT authorship contribution statement

**Dorsa Nezhad Hajian:** Methodology, Software, Writing – original draft. **Fatemeh Parastesh:** Conceptualization, Software, Writing – original draft. **Sajad Jafari:** Conceptualization, Methodology, Validation, Writing – review & editing. **Matjaž Perc:** Conceptualization, Supervision, Writing – review & editing. **Eva Klemenčič:** Conceptualization, Validation, Visualization, Writing – review & editing.

## Declaration of competing interest

The authors declare that they have no known competing financial interests or personal relationships that could have appeared to influence the work reported in this paper.

## Data availability

No data was used for the research described in the article.

## Acknowledgments

M.P. is supported by the Slovenian Research and Innovation Agency (Javna agencija za znanstvenoraziskovalno in inovacijsko dejavnost Republike Slovenije) (Grant Nos. P1-0403 and N1-0232). The work is also partially funded by Centre for Nonlinear Systems, Chennai Institute of Technology, India vide funding number CIT/CNS/2023/RP/012.

## References

[1] Hempel H, Schimansky-Geier L, García-Ojalvo J. Noise-sustained pulsating patterns and global oscillations in subexcitable media. Phys Rev Lett 1999;82(18):3713–6. http://dx.doi.org/10.1103/PhysRevLett.82.3713.

[2] Ullner E, Zaikin A, García-Ojalvo J, Báscones R, Kurths J. Vibrational resonance and vibrational propagation in excitable systems. Phys Lett A 2003;312(5):348–54. http://dx.doi.org/10.1016/S0375-9601(03)00681-9.

[3] Riecke H, Madruga S. Geometric diagnostics of complex patterns: Spiral defect chaos. Chaos 2006;16(1):013125. http://dx.doi.org/10.1063/1.2171515.

[4] Kundu S, Majhi S, Muruganandam P, Ghosh D. Diffusion induced spiral wave chimeras in ecological system. Eur Phys J Spec Top 2018;227:983–93. http://dx.doi.org/10.1140/epjst/e2018-800011-1.

[5] Elkin Y, Biktashev V, Holden A. On the movement of excitation wave breaks. Chaos Solit Fractals 1998;9(9):1597–610. http://dx.doi.org/10.1016/S0960-0779(97)00111-2.

[6] Barton S. Chaos, self-organization, and psychology. Am Psychol 1994;49(1):5–14. http://dx.doi.org/10.1037/0003-066X.49.1.5.

[7] Gomez-Marin A, Garcia-Ojalvo J, Sancho JM. Self-sustained spatiotemporal oscillations induced by membrane-bulk coupling. Phys Rev Lett 2007;98(16):168303. http://dx.doi.org/10.1103/PhysRevLett.98.168303.

[8] Ullner E, Politi A. Self-sustained irregular activity in an ensemble of neural oscillators. Phys Rev X 2016;6(1):011015. http://dx.doi.org/10.1103/PhysRevX.6.011015.

[9] Barkley D, Kness M, Tuckerman LS. Spiral-wave dynamics in a simple model of excitable media: The transition from simple to compound rotation. Phys Rev A 1990;42(4):2489–92. http://dx.doi.org/10.1103/PhysRevA.42.2489.
[10] Pertsov AM, Davidenko JM, Salomonsz R, Baxter WT, Jalife J. Spiral waves of excitation underlie reentrant activity in isolated cardiac muscle. Circ Res 1993;72(3):631–50. http://dx.doi.org/10.1161/01.RES.72.3.631.
[11] Jalife J, Berenfeld O, Skanes A, Mandapati R. Mechanisms of atrial fibrillation: mother rotors or multiple daughter wavelets, or both? J Cardiovasc Electrophysiol 1998;9(8 Suppl):S2–12.
[12] Witkowski FX, Leon LJ, Penkoske PA, Giles WR, Spano ML, Ditto WL, et al. Spatiotemporal evolution of ventricular fibrillation. Nature 1998;392(6671):78–82. http://dx.doi.org/10.1038/32170.
[13] Tranquillo J, Howes M. Intrinsic inhomogeneities and the coexistence of spirals with different periods of rotation. Phys Rev E 2008;78(5):051914. http://dx.doi.org/10.1103/PhysRevE.78.051914.
[14] Majhi S, Bera BK, Ghosh D, Perc M. Chimera states in neuronal networks: A review. Phys Life Rev 2019;28:100–21. http://dx.doi.org/10.1016/j.plrev.2018.09.003.
[15] Kuklik P, Szumowski L, Sanders P, Żebrowski J. Spiral wave breakup in excitable media with an inhomogeneity of conduction anisotropy. Comput Biol Med 2010;40(9):775–80. http://dx.doi.org/10.1016/j.compbiomed.2010.07.005.
[16] Quan W, Rudy Y. Unidirectional block and reentry of cardiac excitation: a model study. Circ Res 1990;66(2):367–82. http://dx.doi.org/10.1161/01.RES.66.2.367.
[17] Roxin A, Riecke H, Solla SA. Self-sustained activity in a small-world network of excitable neurons. Phys Rev Lett 2004;92:198101. http://dx.doi.org/10.1103/PhysRevLett.92.198101.
[18] Riecke H, Roxin A, Madruga S, Solla SA. Multiple attractors, long chaotic transients, and failure in small-world networks of excitable neurons. Chaos 2007;17(2):026110. http://dx.doi.org/10.1063/1.2743611.
[19] Xu C, Tang X, Lü H, Alfaro-Bittner K, Boccaletti S, Perc M, et al. Collective dynamics of heterogeneously and nonlinearly coupled phase oscillators. Phys Rev Res 2021;3(4):043004. http://dx.doi.org/10.1103/PhysRevResearch.3.043004.
[20] Franović I, Todorović K, Vasović N, Burić N. Spontaneous formation of synchronization clusters in homogenous neuronal ensembles induced by noise and interaction delays. Phys Rev Lett 2012;108(9):094101. http://dx.doi.org/10.1103/PhysRevLett.108.094101.
[21] Kuklik P, Żebrowski JJ. Reentry wave formation in excitable media with stochastically generated inhomogeneities. Chaos 2005;15(3):033301. http://dx.doi.org/10.1063/1.1947427.
[22] Etémé A, Tabi C, Mohamadou A, Kofané T. Elimination of spiral waves in a two-dimensional Hindmarsh–Rose neural network under long-range interaction effect and frequency excitation. Physica A 2019;533:122037. http://dx.doi.org/10.1016/j.physa.2019.122037.
[23] He D, Hu G, Zhan M, Ren W, Gao Z. Pattern formation of spiral waves in an inhomogeneous medium with small-world connections. Phys Rev E 2002;65(5):055204. http://dx.doi.org/10.1103/PhysRevE.65.055204.
[24] Ding Q, Wu Y, Yu D, Li T, Jia Y. Inter-layer propagation of spiral waves: Effects of time-varying defect blocks and magnetic flows. Phys Lett A 2023;489:129154. http://dx.doi.org/10.1016/j.physleta.2023.129154.
[25] Ma J, Wang C-N, Tang J, Jia Y. Eliminate spiral wave in excitable media by using a new feasible scheme. Commun Nonlinear Sci Numer Simul 2010;15(7):1768–76. http://dx.doi.org/10.1016/j.cnsns.2009.07.013.
[26] Franović I, Omel'chenko OE, Wolfrum M. Phase-sensitive excitability of a limit cycle. Chaos 2018;28(7):071105. http://dx.doi.org/10.1063/1.5045179.
[27] Franović I, Perc M, Todorović K, Kostić S, Burić N. Activation process in excitable systems with multiple noise sources: Large number of units. Phys Rev E 2015;92(6):062912. http://dx.doi.org/10.1103/PhysRevE.92.062912.
[28] Wang Z, Rostami Z, Jafari S, Alsaadi FE, Slavinec M, Perc M. Suppression of spiral wave turbulence by means of periodic plane waves in two-layer excitable media. Chaos Solit Fractals 2019;128:229–33. http://dx.doi.org/10.1016/j.chaos.2019.07.045.
[29] Li B-W, Zhang H, Ying H-P, Hu G. Coherent wave patterns sustained by a localized inhomogeneity in an excitable medium. Phys Rev E 2009;79(2):026220. http://dx.doi.org/10.1103/PhysRevE.79.026220.
[30] Kuklik P, Wong CX, Brooks AG, Jacek Żebrowski J, Sanders P. Role of spiral wave pinning in inhomogeneous active media in the termination of atrial fibrillation by electrical cardioversion. Comput Biol Med 2010;40(3):363–72. http://dx.doi.org/10.1016/j.compbiomed.2010.02.001.
[31] Zhang J, Tang J, Ma J, Luo JM, Yang XQ. The dynamics of spiral tip adjacent to inhomogeneity in cardiac tissue. Physica A 2018;491:340–6. http://dx.doi.org/10.1016/j.physa.2017.09.051.
[32] Mesin L. Dynamics of spiral waves in a cardiac electromechanical model with a local electrical inhomogeneity. Chaos Solit Fractals 2012;45(9):1220–30. http://dx.doi.org/10.1016/j.chaos.2012.05.013.
[33] Lim ZY, Maskara B, Aguel F, Emokpae R, Tung L. Spiral wave attachment to millimeter-sized obstacles. Circ 2006;114(20):2113–21. http://dx.doi.org/10.1161/CIRCULATIONAHA.105.598631.
[34] Ikeda T, Yashima M, Uchida T, Hough D, Fishbein MC, Mandel WJ, et al. Attachment of meandering reentrant wave fronts to anatomic obstacles in the atrium. Circ Res 1997;81(5):753–64. http://dx.doi.org/10.1161/01.RES.81.5.753.
[35] Tanaka M, Hörning M, Kitahata H, Yoshikawa K. Elimination of a spiral wave pinned at an obstacle by a train of plane waves: Effect of diffusion between obstacles and surrounding media. Chaos 2015;25(10):103127. http://dx.doi.org/10.1063/1.4934561.
[36] Majumder R, Zykov VS, Panfilov AV. In silico optical control of pinned electrical vortices in an excitable biological medium. New J Phys 2020;22(2):023034. http://dx.doi.org/10.1088/1367-2630/ab704f.
[37] Kitanov PM, LeBlanc VG. Dynamics of meandering spiral waves with weak lattice perturbations. SIAM J Appl Dyn Syst 2017;16(1):16–53. http://dx.doi.org/10.1137/16M1080483.
[38] Hendrey M, Ott E, Antonsen TM. Spiral wave dynamics in oscillatory inhomogeneous media. Phys Rev E 2000;61:4943–53. http://dx.doi.org/10.1103/PhysRevE.61.4943.
[39] Hussaini S, Venkatesan V, Biasci V, Romero Sepúlveda JM, Quiñonez Uribe RA, Sacconi L, et al. Drift and termination of spiral waves in optogenetically modified cardiac tissue at sub-threshold illumination. eLife 2021;10:e59954. http://dx.doi.org/10.7554/eLife.59954.
[40] Nizamieva AA, Kalita IY, Slotvitsky MM, Berezhnoy AK, Shubina NS, Frolova SR, et al. Conduction of excitation waves and reentry drift on cardiac tissue with simulated photocontrol-varied excitability. Chaos 2023;33(2):023112. http://dx.doi.org/10.1063/5.0122273.
[41] Yuan G, Zhang H, Xu A, Wang G. Attractive and repulsive contributions of localized excitability inhomogeneities and elimination of spiral waves in excitable media. Phys Rev E 2013;88(2):022920. http://dx.doi.org/10.1103/PhysRevE.88.022920.
[42] Wu X, Ma J, Li F, Jia Y. Development of spiral wave in a regular network of excitatory neurons due to stochastic poisoning of ion channels. Commun Nonlinear Sci Numer Simul 2013;18(12):3350–64. http://dx.doi.org/10.1016/j.cnsns.2013.05.011.
[43] Lindner B, Schimansky-Geier L. Analytical approach to the stochastic FitzHugh-Nagumo system and coherence resonance. Phys Rev E 1999;60(6):7270–6. http://dx.doi.org/10.1103/PhysRevE.60.7270.
[44] Lindner B, Schimansky-Geier L. Coherence and stochastic resonance in a two-state system. Phys Rev E 2000;61:6103–10. http://dx.doi.org/10.1103/PhysRevE.61.6103.
[45] Majhi S, Ghosh D. Alternating chimeras in networks of ephaptically coupled bursting neurons. Chaos 2018;28(8):083113. http://dx.doi.org/10.1063/1.5022612.
[46] Ding Q, Wu Y, Hu Y, Liu C, Hu X, Jia Y. Tracing the elimination of reentry spiral waves in defibrillation: Temperature effects. Chaos Solit Fractals 2023;174:113760. http://dx.doi.org/10.1016/j.chaos.2023.113760.
[47] Ma J, Wang Y, Wang C, Xu Y, Ren G. Mode selection in electrical activities of myocardial cell exposed to electromagnetic radiation. Chaos Solit Fractals 2017;99:219–25. http://dx.doi.org/10.1016/j.chaos.2017.04.016.
[48] Hwang S-M, Kim TY, Lee KJ. Complex-periodic spiral waves in confluent cardiac cell cultures induced by localized inhomogeneities. Proc Natl Acad Sci 2005;102(29):10363–8. http://dx.doi.org/10.1073/pnas.0501539102.
[49] Davidenko JM, Pertsov AV, Salomonsz R, Baxter W, Jalife J. Stationary and drifting spiral waves of excitation in isolated cardiac muscle. Nature 1992;355(6358):349–51. http://dx.doi.org/10.1038/355349a0.
[50] Ong JJ, Cha YM, Kriett JM, Boyce K, Feld GK, Chen PS. The relation between atrial fibrillation wavefront characteristics and accessory pathway conduction. J Clin Invest 1995;96(5):2284–96. http://dx.doi.org/10.1172/JCI118284.
[51] Cabo C, Pertsov AM, Baxter WT, Davidenko JM, Gray RA, Jalife J. Wave-front curvature as a cause of slow conduction and block in isolated cardiac muscle. Circ Res 1994;75(6):1014–28. http://dx.doi.org/10.1161/01.RES.75.6.1014.